

# MODELLING OF GIMBAL CONTROL MOMENT GYRO AND ANALYSIS OF GIMBAL DISTURBANCE IMPACT

Xue Li, Wei Cheng, Xiongfei Li

Original scientific paper

Control Moment Gyroscope is one of the main sources of disturbance affecting the accuracy of attitude control system in the spacecraft. This paper concentrates on analysing and testing the micro-vibrations produced by CMG. To analyse its disturbance features systematically, the mechanical features of flywheel, frame and the entire CMG will be firstly studied, and then the kinetics model of CMG will be established. The structure patterns of disturbance sources, including mass imbalance and bearings irregularity, are taken into account in this model. Thirdly, the micro-vibration dynamic testing of CMG would be implemented by using originally designed eight-axial test board, including dynamic tests under multiple frame rotation speed. Finally, comparison will be demonstrated between the measured disturbance features from the experiment and the calculated theoretical model results to validate the model. Therefore, the model presented here can be employed to predict the micro-vibration characteristics of a CMG.

**Keywords:** CMG, disturbance characteristics test, gimbal disturbance, vibration analysis

## Modeliranje giroskopskog upravljačkog momenta i analiza utjecaja smetnji na kardanskom prstenu

Izvorni znanstveni članak

Giroskopski upravljački moment (CMG) je jedan od glavnih izvora smetnji koje utječu na točnost upravljačkog sustava položaja letjelice. Rad je usmjeren na analizu i ispitivanje mikro-vibracija koje proizvodi CMG. U cilju sistematske analize smetnji, najprije će se analizirati mehaničke značajke zamašnjaka, okvir i čitav CMG, a tada će se uspostaviti kinetički model CMG-a. U tom su modelu uzeti u obzir strukturni uzorci izvora smetnji, uključujući neravnotežu mase i nepravilnost ležaja. Treće, izvršilo bi se dinamičko ispitivanje mikro vibracija CMG-a primjenom originalno konstruirane osmo-aksijalne probne ploče, uključujući dinamička ispitivanja pri višestrukim brzinama rotacije okvira. Konačno, demonstrirat će se usporedba između karakteristika smetnji izmijerenih eksperimentom i izračunatih rezultata teorijskog modela u svrhu potvrde modela. Prema tome, model predstavljen ovdje, može se koristiti za predviđanje karakteristika mikro-vibracija CMG-a.

**Ključne riječi:** analiza vibracija, CMG, ispitivanje karakteristika smetnji, smetnje kardanskog prstena

## 1 Introduction

As an actuator of spacecraft attitude control, Control Moment Gyroscope (CMG) produces significant output torque and exhibits excellent control linearity, anti-disturbance, and rapid response features. Therefore, CMG is the preferred actuator for long-life spacecraft. For mass imbalance, bearing manufacturing defects, electrical motor noises, and other factors, however, the CMG produces periodic and broadband disturbed vibration to the spacecraft while controlling torque. This disturbance force is modulated and magnified through internal dynamic mechanisms. The CMG also significantly affects the pointing precision of the optical path and the stability of the remote sensing satellite [1, 16].

Although R/MWAs and CMG, the most prominent sources of disturbance, both achieve reaction torque via high speed rotary flywheels, their operating principles are different from each other [1]. R/MWAs provide control torque for spacecraft by adjusting the rotational acceleration of the flywheel, which operates at nominal zero (RWA) or non-zero (MWA) bias velocity [3, 4]. CMG generates gyroscopic torques by gimbaling the angular momentum vector of the flywheel, which is gimballed and usually operates with a constant rotating speed that is much larger than the maximum of the R/MWA (as high as  $6000 \div 10\,000$  rev/min) [2].

The CMG achieves spacecraft attitude change through the angular momentum change of the flywheel which is forced by frame rotation. The major disturbance to the flywheel would be generated from below: flywheel mass imbalance, internal resonance, imperfection in mechanical bearings and motor ripple. A number of

studies have investigated the disturbances produced by rotary flywheels.

Most papers published focus on disturbance produced by flywheel mass imbalance and consider it as the largest disturbance source or analyse the disturbance sources separately [4  $\div$  8, 14  $\div$  15, 17]. The amplitudes of disturbance forces and torques, originating from the imbalance of mass distribution, are highly coherent to the square of the angular velocity. Meanwhile, due to fundamental harmonic, the frequency of disturbance is equal to the rotation frequency. Internal resonance would take place while the disturbance harmonics crossing the flywheel structural modes, a phenomenon raised by Masterson et al. [7] and a linear flywheel dynamic model, with five degrees of freedom for the RWA, is created to capture the interaction between the structural modes and fundamental harmonic. Additional stimulant, brought from the bearings which support the flywheel, is introduced due to imperfections of the retainer. A sub-harmonic, with an approximately 0,6 times fundamental harmonic frequency, is found by Shigemune and Yoshiaki [6] for the imperfections of the nonholonomically constrained bearing retainer. The rotation elements and raceways of the bearings provide compliant mechanism support, which allows the flywheel to translate rock and amplify the disturbance force and torque. Furthermore, in high rotation speed, non-linear elastic contact and clearance in the bearing assemblies would always result in nonlinearities.

Several methods, which were used to measure the micro-vibrations produced from the flywheel, have already been studied and evaluated. For example, Elias and Miller [12] have proposed a coupled disturbances

analysis method using dynamic mass measurement techniques. Shigemune, Yoshiaki, and Masahito et al. [6, 13] have established a method to measure lower frequency disturbances induced by WAs, which are traditionally difficult to detect, and revealed that the inner dynamics of the WA closely relate to the disturbances. Zhou et al. [14] have proposed a cost-effective measurement system consisting of a seismic mass and two high sensitive accelerometers, which has been used to test the micro-vibrations produced by a cantilevered momentum wheel assemblies.

Currently, there are few references studying the micro-vibration of CMG, especially for the micro-vibration under rotating CMG frame. In this paper, both dynamic modelling and experimental testing are conducted to study the disturbances generated by CMG. Firstly, this paper establishes the model by implementing Euler Equations separately for the flywheel and frame, and studies the kinetics relationships of CMG components. Furthermore, this paper measures the disturbance feature of CMG under multiple frame rotation speed by implementing the eight-component test board, which is designed specifically for this experiment. Finally, this paper compares the disturbance characteristics obtained with the test and verifies the accuracy of the theoretical model.

The following Section 2 provides the modelling details of the theoretical model for CMG and analyses the disturbance sources from CMG. Section 3 gives the details of the experimental test. Section 4 represents and discusses the results obtained by experiment. At last, Section 5 summarizes the paper and presents the conclusion.

## 2 CMG kinetics model

### 2.1 System description and the coordinate systems

The main rotation components of single frame CMG, including the rotor and frame. The rotor rotates rapidly corresponding to the frame, which is slowly rotating to the foundation. The simplified mechanics model of CMG is shown in Fig 1. The preconditions of the model include: the rotational angular momentum of flywheel is far greater than the non-rotational angular momentum, and all components of the execution device are rigid.

Since the kinematics of CMG micro-dynamic system is complicated, the following coordinates need to be introduced:

$OXYZ$  is an inertial frame fixed in space. The origin O is at the centre of mass of the gimbal-bearing system, and the OY-axis is in line with the gimbal axis.

$Ox_gy_rz_r$ - is an inertial frame defined in the interface between the SGCMG and the mounting surface.

$Ox_by_bz_b$  - the origin O is set to be the centre of mass of flywheel-bearing system, and the  $Oy_b$  is along the spinning axis.

$Ox_gy_gz_g$  - is the gimbal-fixed frame, which vibrates and rotates along with the gimbal-bearing system. The origin O is fixed to the centre of mass of the gimbal-bearing system, and the  $Oy_g$  is in line with the gimbal axis.  $Ox_gy_gz_g$  coincides with the frame  $OXYZ$  at the initial time.

$Ox_gy_rz_r$ - is the rocking frame of the flywheel with the origin O gimbal-fixed to the centre of mass of the flywheel-bearing system, and the  $Oy_r$  is along the spinning axis.

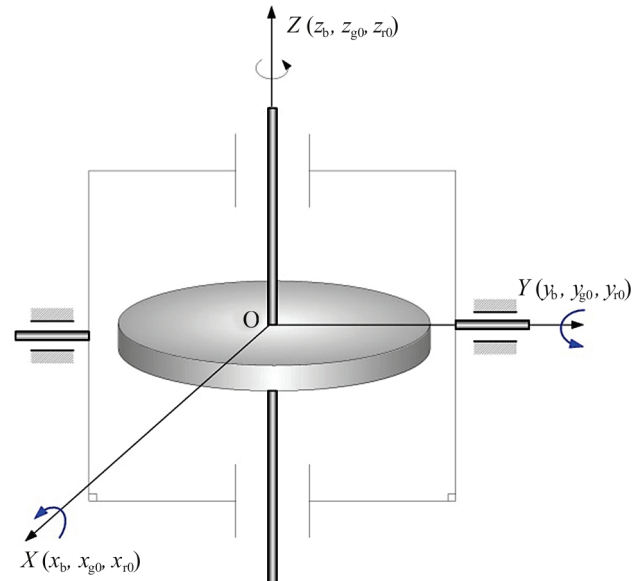


Figure 1 The simplified mechanics model of CMG

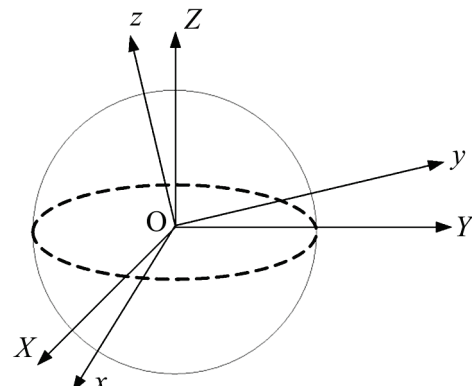


Figure 2 Rigid-connected movement coordinate system

### 2.2 Modelling method

In this section, the motion differential equation could be derived from Euler's Dynamics Equation. Firstly, the Euler's Dynamics Equation of rigid-connected rotation could be shown in Eq. (1) and Fig. 2.

$$\begin{cases} \frac{dH_x}{dt} + \omega_y H_z + \omega_z H_y = M_x \\ \frac{dH_y}{dt} + \omega_z H_x + \omega_x H_z = M_y \\ \frac{dH_z}{dt} + \omega_x H_y + \omega_y H_x = M_z \end{cases} \quad (1)$$

where  $OXYZ$  is the inertial coordinates system, and  $OXYZ$  is rigid-connected coordinate system;  $H_x$ ,  $H_y$  and  $H_z$  are the projections of rigid angular momentum respectively to axes of  $OX$ ,  $OY$  and  $OZ$ ;  $\omega_x$ ,  $\omega_y$  and  $\omega_z$  are the projections of rigid angular speed corresponding to axes of  $OX$ ,  $OY$  and  $OZ$ ;  $M_x$ ,  $M_y$  and  $M_z$  are the projections of external torques corresponding to axes of  $OX$ ,  $OY$  and  $OZ$ .

### 2.2.1 Kinetics model of the flywheel

Flywheel is the core functioning unit of CMG, so the rotor's kinetics model is playing an important role in CMG studying. Considering the rigidity and damping features of rotor bearings, the rotor kinetics model could be established as below. It is assumed that the rotation movement of bearings to the rotor is symmetric to the original point of rotor's coordinate system, as is shown in Fig. 3.

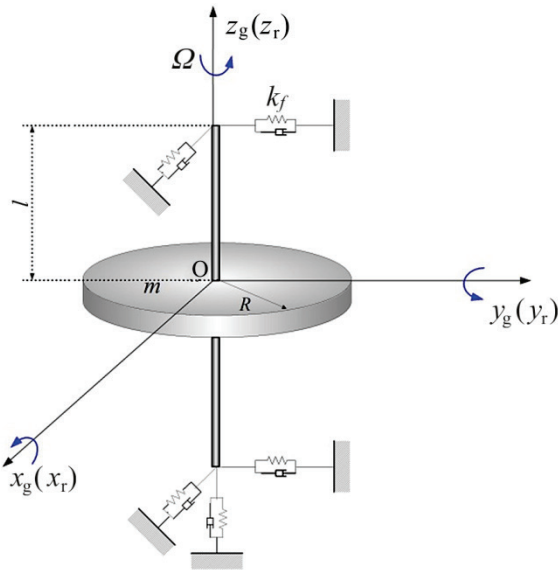


Figure 3 Simplified mechanics model of high speed Flywheel

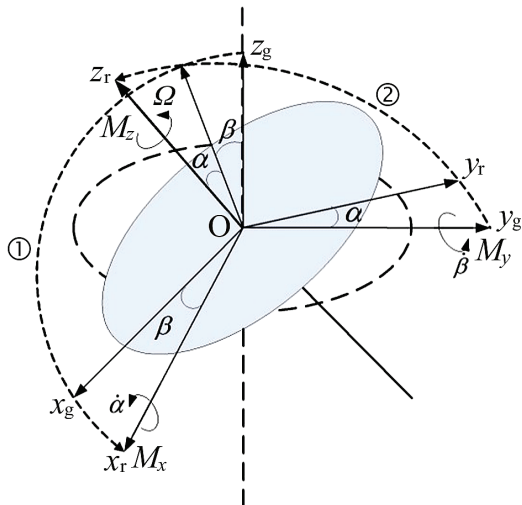


Figure 4 The rotation of flywheel coordinate system  $Ox_r y_r z_r$  corresponding to the frame coordinate system  $Ox_g y_g z_g$

According to the kinematics' principle, the rotation movement of flywheel to the frame could be regarded as the synthesis of autorotation and other two rotations of different directions. The vector of rotor's angular speed to the frame is assumed to be  $\omega$ :

$$\omega = \Omega + \dot{\alpha} + \dot{\beta}, \quad (2)$$

assuming the angular speed vector of the rotor in its own coordinate system is  $\omega_r$ , and its projections in  $Ox_r$ ,  $Oy_r$  and  $Oz_r$  axis are  $\omega_{rx}$ ,  $\omega_{ry}$  and  $\omega_{rz}$ . Therefore, we could get  $\omega_r$  from the projection in Fig. 3 as the following:

$$\omega_r = \begin{bmatrix} \omega_{rx} \\ \omega_{ry} \\ \omega_{rz} \end{bmatrix} = \begin{bmatrix} \dot{\alpha} \\ \dot{\beta} \cos \alpha \\ \Omega - \dot{\beta} \sin \alpha \end{bmatrix}, \quad (3)$$

assuming the rotor's inertia matrix corresponding to  $Ox_r$ ,  $Oy_r$  and  $Oz_r$  is  $J_r$ , and that

$$J_r = \begin{pmatrix} J_{xx} & 0 & 0 \\ 0 & J_{yy} & 0 \\ 0 & 0 & J_{zz} \end{pmatrix}. \quad (4)$$

And the angular momentum vector of rotor is  $H_r$ :

$$H_r = \begin{bmatrix} J_{xx}\omega_{rx} \\ J_{yy}\omega_{ry} \\ J_{zz}\omega_{rz} \end{bmatrix} = \begin{bmatrix} J_{xx}\dot{\alpha} \\ J_{yy}\dot{\beta} \cos \alpha \\ J_{zz}(\Omega - \dot{\beta} \sin \alpha) \end{bmatrix}. \quad (5)$$

Based on the above assumptions, we suppose the external torque of the rotor corresponding to the frame is  $M_r$ , and then according to the moment of momentum theory, we will get:

$$M_r = \frac{\partial H}{\partial t} + \omega \times H_r, \quad (6)$$

assuming that  $M_r$ 's projections to  $Ox_r$ ,  $Oy_r$  and  $Oz_r$  are respectively  $M_{rx}$ ,  $M_{ry}$  and  $M_{rz}$ , which could be interpreted as  $M_r = (M_{rx} \ M_{ry} \ M_{rz})^T$ .

By implementing Eq. (1), the rotary differential equation of the rotor would be:

$$\begin{cases} M_{rx} = J_{xx}\ddot{\alpha} + J_{zz}(\Omega - \dot{\beta} \sin \alpha)\dot{\beta} \cos \alpha + \\ + J_{yy}\dot{\beta}^2 \sin \alpha \cos \alpha \\ M_{ry} \cos \alpha = J_{yy}\ddot{\beta} \cos \alpha - J_{zz}\dot{\alpha}\dot{\beta} \sin \alpha - \\ - J_{zz}\dot{\alpha}(\Omega - \dot{\beta} \sin \alpha) \\ M_{rz} - M_{ry} \sin \alpha = \\ = J_{zz}(\Omega - \dot{\beta} \sin \alpha - \dot{\alpha}\dot{\beta} \cos \alpha) \end{cases}, \quad (7)$$

assuming the rotor's projections of its external force to  $Ox_g$ ,  $Oy_g$  and  $Oz_g$  are respectively  $f_{gx}$ ,  $f_{gy}$  and  $f_{gz}$ . According to the motion law of mass centre, the translational Kinetics model would be:

$$\begin{cases} f_{gx} = m\ddot{x} \\ f_{gy} = m\ddot{y} \\ f_{gz} = m\ddot{z} \end{cases} \quad (8)$$

Combining the Eq. (7) with Eq. (8), the rotor's Kinetics model equations would be:

$$\begin{cases} f_{gx} = m\ddot{x} \\ f_{gy} = m\ddot{y} \\ f_{gz} = m\ddot{z} \\ M_{rx} = J_{xx}\ddot{\alpha} + J_{zz}(\Omega - \dot{\beta}\sin\alpha)\dot{\beta}\cos\alpha + \\ + J_{yy}\dot{\beta}^2\sin\alpha\cos\alpha \\ M_{ry} \cos\alpha = J_{yy}\dot{\beta}\cos\alpha - J_{zz}\dot{\alpha}\dot{\beta}\sin\alpha - \\ - J_{zz}\dot{\alpha}(\Omega - \dot{\beta}\sin\alpha) \\ M_{rz} - M_{ry} \sin\alpha = \\ = J_{zz}(\Omega - \dot{\beta}\sin\alpha - \dot{\alpha}\dot{\beta}\cos\alpha) \end{cases} \quad (9)$$

## 2.2.2 Kinetics model of the gimbal

Gimbal is one of CMG's components with low rotation speed. Similar to the flywheel, the model is established by simplifying the exact gimbal structure. And considering the force exerted from the flywheel to the gimbal as the external excitement, the simplified mechanics model would be:

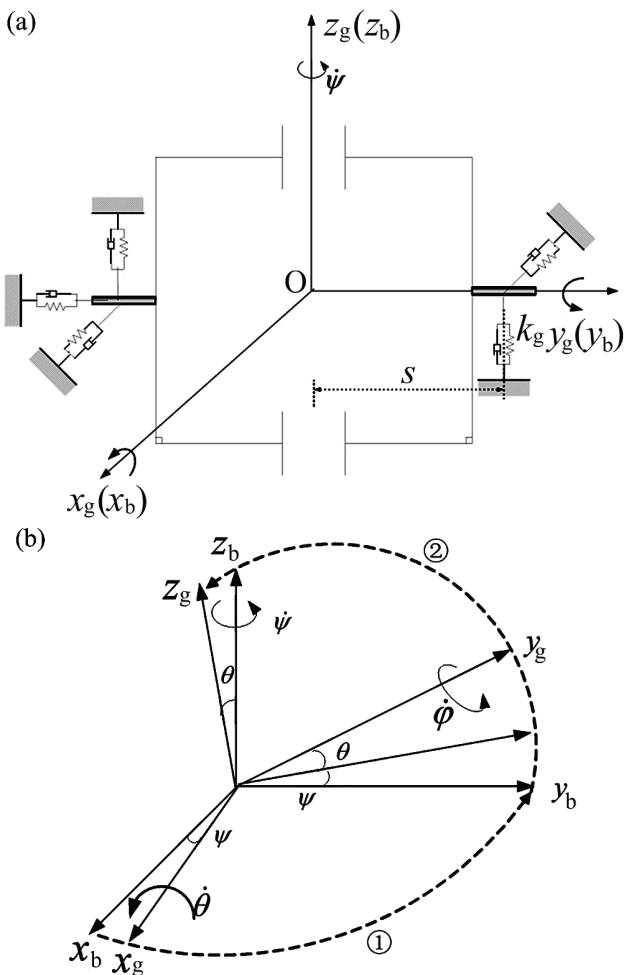


**Figure 5** (a) Simplified gimbal mechanics model (b): The rotation relationships between frame coordinate system  $Ox_g y_g z_g$  and base coordinate system  $Ox_b y_b z_b$

And for the gimbal kinetics model equations, which are similar to the flywheel model, it could be expressed as:

$$\begin{cases} f_{bx} = m_g\ddot{x} \\ f_{by} = m_g\ddot{y} \\ f_{bz} = m_g\ddot{z} \\ M_{gx} = J_{gxx}\ddot{\theta} + J_{gxy}(\dot{\phi} + \psi\sin\theta)\dot{\psi}\cos\theta + \\ + J_{gzz}\dot{\psi}^2\sin\theta\cos\theta \\ M_{gy} - M_{gz}\sin\theta = \\ = J_{gyy}(\dot{\phi} + \dot{\psi}\sin\theta + \dot{\psi}\theta\cos\theta) \\ M_{gz}\cos\theta = J_{gzz}\dot{\psi}\cos\theta - J_{gyy}\psi\dot{\theta}\sin\theta - \\ - J_{gyy}\dot{\theta}(\dot{\phi} + \dot{\psi}\sin\theta) \end{cases} \quad (10)$$

In the above equation,  $J_{gxx}$ ,  $J_{gyy}$  and  $J_{gzz}$  are respectively the rotary inertia of the three axes. And the external force of frame in the three axes are  $f_{bx}$ ,  $f_{by}$  and  $f_{bz}$ , the projections of external torque vector, which include  $Ox_g$ ,  $Oy_g$  and  $Oz_g$ , are  $M_{gx}$ ,  $M_{gy}$ ,  $M_{gz}$ , respectively.

## 2.2.3 Entire kinetics model of the CMG

To get the kinetics model of entire CMG, the simplification of rotary equations needs to be implemented. For the two orthogonal directions of the flywheel and gimbal's axis rotation, the rotary angular is quite small, which means  $\alpha$ ,  $\beta$ ,  $\theta$  and  $\psi$  are all insignificantly small, then we could have the following assumptions:  $\sin\alpha \rightarrow 0$ ,  $\cos\alpha \rightarrow 1$ ,  $\sin\beta \rightarrow 0$ ,  $\cos\beta \rightarrow 1$ ,  $\sin\theta \rightarrow 0$ ,  $\cos\theta \rightarrow 1$ ,  $\sin\psi \rightarrow 0$  and  $\cos\psi \rightarrow 1$ . Then we could get a simplified Eq. (8) with higher order terms ignored:

$$\begin{cases} f_{gx} = m\ddot{x} \\ f_{gy} = m\ddot{y} \\ f_{gz} = m\ddot{z} \\ M_{rx} = J\ddot{\alpha} + 2J\Omega\dot{\beta} \\ M_{ry} = J\ddot{\beta} - 2J\Omega\dot{\alpha} \\ M_{rz} = 2J\dot{\Omega} \end{cases} \quad (11)$$

Within Eq. (11),  $J = J_{xx} = J_{yy} = \frac{1}{2}J_{zz}$ . And the frame kinetics model could be simplified as:

$$\begin{cases} f_{bx} = m_g\ddot{x} \\ f_{by} = m_g\ddot{y} \\ f_{bz} = m_g\ddot{z} \\ M_{gx} = J_{gxx}\ddot{\theta} + H_{gy}\dot{\psi} \\ M_{gy} = J_{gyy}\dot{\phi} \\ M_{gz} = J_{gzz}\dot{\psi} - H_{gy}\dot{\theta} \end{cases} \quad (12)$$

To get the entire CMG's kinetics equations, Eq. (12) needs to be further analysed. Without external disturbance, the torque of the gimbal could be separated into two parts: torque exerted to the gimbal from the foundation, which is named  $M_{bg}^g$ , and the torque from the

high speed flywheel, which is named  $M_{rg}^g$ . It could be concluded that  $M^g = M_{bg}^g + M_{rg}^g$ , and  $M_{bg}^g = [M_{bgx}^g \ M_{bgy}^g \ M_{bgz}^g]^T$ . The gimbal coordinate system would be implemented as the reference coordinate system for all the vectors. Due to the flywheel and stator of the motor are gimbal-fixed respectively to the high speed flywheel and gimbal, it could be concluded that the impact between CMG flywheel and gimbal is implemented through the motor and bearings. There exists a pair of counter-torque: the external torque of the high speed flywheel and the torque exerted from the rotor to the gimbal. If we suppose the torque exerted from the flywheel to the gimbal is  $M_r^g$ , then we will achieve:

$$M_r = -M_r^g. \quad (13)$$

In Eq. (13), all the vectors implement the flywheel reference coordinate system. According to Fig. 5, the transition matrix  $C_g^r$  from rotor coordinate to gimbal coordinate system could be get:

$$M_{rg}^g = C_g^{r-1} M_r^g = -C_g^{r-1} M^r. \quad (14)$$

Taking all above equations into account, the kinetics model of the whole CMG could be:

$$\begin{cases} f_{bgx}^g = m_g \ddot{x} + f_{rgx}^g \\ f_{bgy}^g = m_g \ddot{y} + f_{rgy}^g \\ f_{bgz}^g = m_g \ddot{z} + f_{rgz}^g \\ M_{bgx}^g = J_{gxx} \ddot{\theta} + H_{gy} \dot{\psi} - J \ddot{\alpha} - 2J\Omega \dot{\beta} - 2J\dot{\Omega} \beta. \\ M_{bgy}^g = J_{gyy} \ddot{\phi} - J \ddot{\beta} + 2J\Omega \dot{\alpha} + 2J\dot{\Omega} \alpha \\ M_{bgz}^g = J_{gzz} \ddot{\psi} - H_{gy} \dot{\theta} = \\ = J \ddot{\alpha} \beta + 2J\Omega \dot{\beta} \beta - J \ddot{\beta} \alpha + 2J\Omega \dot{\alpha} \alpha - 2J\dot{\Omega} \end{cases} \quad (15)$$

where  $(f_{rgx}^g \ f_{rgy}^g \ f_{rgz}^g)^T$  is the force vector exerted to the gimbal at the high speed output position, and  $(f_{bgx}^g \ f_{bgy}^g \ f_{bgz}^g)^T$  is the external force vector of the whole CMG.

### 2.3 The analysis of the CMG disturbing feature

From Eq. (15) we can see that the force and moment outputs by the CMG are determined by the input disturbances. Therefore, we investigate the main disturbance inputs, which are mass imbalance, bearing irregularity and structural modes as follows.

#### 2.3.1 Disturbance from the mass imbalance of the rotation parts

There are two kinds of imbalance feature caused by the flywheel mass imbalance, the static and dynamic

imbalance (Fig. 6). The static imbalance means the mass centre deviates from the rotation axis, and dynamic imbalance means that the imbalance of the flywheel mass distribution would lead to the nonzero accumulated rotation inertia [9]. The force brought from the static imbalance is

$$F_s|_{Ox_r y_r z_r} = [U_s \Omega^2 \cos(\Omega \cdot t + \varphi_s) \ U_s \Omega^2 \sin(\Omega \cdot t + \varphi_s) \ 0]^T, \quad (16)$$

and the torque produced by dynamic imbalance is

$$T_d|_{Ox_r y_r z_r} = [U_d \Omega^2 \cos(\Omega \cdot t + \varphi_d) \ U_d \Omega^2 \sin(\Omega \cdot t + \varphi_d) \ 0]^T. \quad (17)$$

In the above equation,  $U_s = m_s r_s$ ,  $U_d = m_d r_d h_f$ ,  $\varphi_s$  and  $\varphi_d$  are the initial phase.

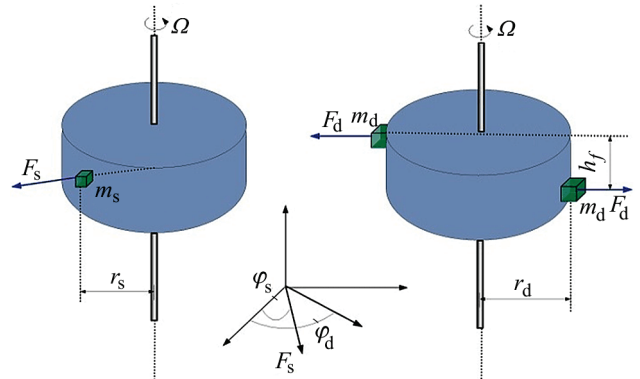


Figure 6 The static and dynamic imbalance of the high speed flywheel

#### 2.3.2 Disturbance from the bearing irregularity

Angular contact ball bearings are widely used in CMG. And it is consisted of internal ring, external ring, rolling elements and Cage. The irregularity of them will introduce disturbances during rotating [11, 18 ÷ 22]. And the angular frequencies of each disturbance can be obtained by analysing the relative motion of each part [4].

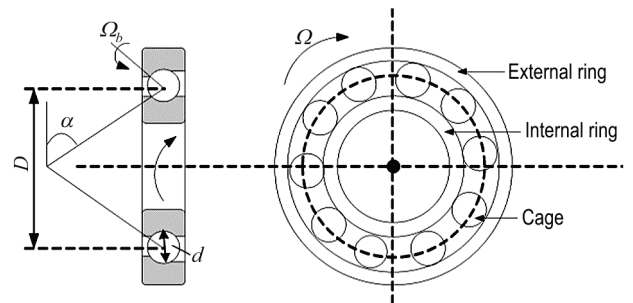


Figure 7 Sketch of angular contact ball bearing

The contact loads between the  $j^{\text{th}}$  rolling balls and the raceways coincide with the elastic deformation function  $\delta_j$ , according to the Hertz elasticity contact theory [18]. And it could be expressed as:

$$f_j = k_j \delta_j^{\frac{3}{2}}. \quad (18)$$

Where  $k_j$  is the contact stiffness coefficient, obtained as

$$k_j = \left[ \frac{1}{\left( \frac{1}{k_{ji}} \right)^{\frac{2}{3}} + \left( \frac{1}{k_{je}} \right)^{\frac{2}{3}}} \right]^{\frac{2}{3}}. \quad (19)$$

Where  $k_{ji}$  and  $k_{je}$  are the stiffness coefficients respectively between the rolling balls and both the internal and external raceway surface. The values of the stiffness coefficients can be calculated using Poisson ratio, Young's modulus and the curvatures of the contact points [19].

The internal ring is stationary, while the external ring is rotating with an angular velocity of  $\Omega$ . Thus, the angular velocity of the cage relative to the internal ring can be expressed as [4]:

$$\Omega_{ci} = 0.5\Omega \left( 1 + \frac{d}{D} \cos \alpha \right). \quad (20)$$

The angular velocity of the cage relative to the external ring can be expressed as

$$\Omega_{ce} = -0.5\Omega \left( 1 - \frac{d}{D} \cos \alpha \right). \quad (21)$$

The angular velocity of the ball can be expressed as

$$\Omega_b = 0.5\Omega \left( \frac{D}{d} - \frac{d}{D} \cos^2 \alpha \right). \quad (22)$$

The angular velocities of the ball passing the internal and external ring can be expressed as

$$\Omega_{bi} = z \frac{1}{n} \Omega_{ci}, \quad (23)$$

$$\Omega_{be} = z \frac{1}{n} \Omega_{ce}. \quad (24)$$

where  $z$  is the number of the balls in the bearing,  $n = 1, 2, \dots, N$ ,  $N$  is the number of bearings in the CMG.

### 2.3.3 Disturbance by the torque of the servo driving system

The gimbal servo system drives the rotary flywheel to rotate to obtain the gyroscopic torques, which is necessary for attitude control of the spacecraft [1]. The driving torque provided by the servo system is along the gimbal axis and can be expressed as

$$T_g|_{Oxyg} = \begin{bmatrix} 0 & M_{bg}^g & 0 \end{bmatrix}^T. \quad (25)$$

$M_{bg}^g$  includes not only the input torque  $T_{input}$ , and other torques are produced by the imperfection of the servo system, which consists of the bearings and motor. When the rotation speed is relatively slow, the friction

torque would impact the frame servo driving system [24]. There are the bearings' solid friction torque and viscous friction torque generated from the lubricant.

$$\frac{dT_{f1}}{dt} = \gamma \left( T_{f1} \frac{\Omega}{|\Omega|} - T_{f0} \right)^2 \Omega, \quad (26)$$

$$T_{f2} = c\Omega.$$

Where  $T_{f1}$  is the solid friction torque of the bearings;  $T_{f0}$  the possible maximized static friction torque;  $T_{f2}$  the viscous friction torque of the lubricant;  $c$  the damping coefficient; and  $\gamma$  is the Dachau model coefficient.

Another disturbing torque is generated from the pulse of the motor torque  $T_{ripple}$ . Normally, the execution components are driven by the brushless DC motor. Therefore, controlling of the components rotation speed could be achieved by altering the motor's rotation speed. And it would be affected by the magnetic flux distribution and servo circuit. Then the  $T_{ripple}$  could be expressed as:

$$T_{ripple} = T_\alpha \sin \frac{n_m}{p_m} \theta_m - T_r (\kappa_5 - \kappa_7) \cos 6\theta_m. \quad (27)$$

Within the above equation,  $T_r$  is the reference torque,  $T_\alpha$  the amplitude of the cogging torque; and  $\kappa_i$  the coefficient of the  $i^{th}$  harmonic component.

So  $M_{bg}^g$  could be interpreted as:

$$M_{bg}^g = T_{input} + T_{friction} + T_{ripple}. \quad (28)$$

### 2.4 Disturbing model of the entire CMG

$k_g$  and  $c_g$  are respectively the radial rigidity and damping of the frame bearings;  $k_{ag}$  and  $c_{ag}$  are the axial rigidity and damping respectively.  $\sum_{i=1}^{\infty} F_{rz_i} e^{j i \Omega t}$  is the axial disturbance of the rotor, and the translational CMG model should be:

$$\begin{cases} (m_g + m) \ddot{x} + k_g x + c_g \dot{x} = \\ = m_s R \cos \Omega t + \sum_{i=2}^n C_i (h_i \Omega)^2 \cos (h_i \Omega t) \\ (m_g + m) \ddot{y} + k_{ag} y + c_{ag} \dot{y} = \\ = m_s R \Omega^2 \sin \Omega t + \sum_{i=2}^n C_i (h_i \Omega)^2 \sin (h_i \Omega t) \\ (m_g + m) \ddot{z} + k_g z + c_g \dot{z} = \sum_{i=1}^{\infty} F_{rz_i} e^{j i \Omega t} \end{cases}. \quad (29)$$

For the  $\Omega$  of CMG is constant value, then  $\dot{\Omega} = 0$ . The span of frame bearings is  $2l_g$ . So the rotational CMG model should be:

$$\begin{cases} J_{gxx}\ddot{\theta} + H_{gy}\dot{\psi} + 2k_g l_g^2 \theta + c_g l_g^2 = J\ddot{\alpha} - 2J\Omega\dot{\beta} \\ J_{gyy}\ddot{\phi} = J\ddot{\beta} - 2J\Omega\dot{\alpha} + T_{\text{input}} + T_{\text{friction}} + T_{\text{ripple}} \\ J_{gzz}\ddot{\psi} - H_{gy}\dot{\theta} + 2k_g l_g^2 \psi + c_g l_g^2 \dot{\psi} = 0 \end{cases} \quad (30)$$

### 3 Experiment test

#### 3.1 Experimental set-up

The micro-vibrations test was conducted in a measurement system consisting of Rigid eight-axis test board and optical tabletop. A series of tests were carried out with the purpose to measure the micro-vibrations emitted by the CMG and to validate the mechanical model derived in the previous section. The spinning speed of the flywheel was set at a constant 9500 rpm/min during the test.

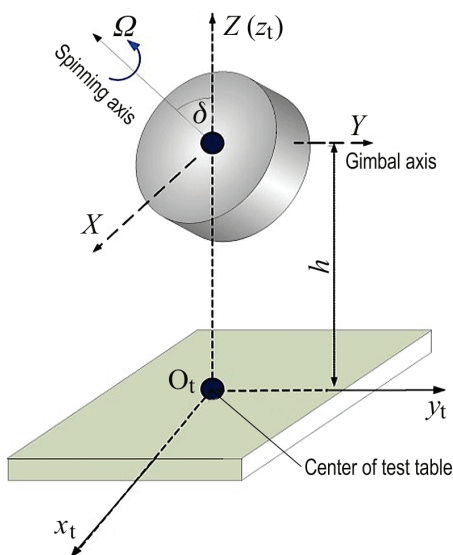


Figure 8 Measuring coordinates arrangement of the experimental set-up

Table 1 Specification of the off-the-shelf SGCMG

Parameters	Notation	Value
Angular momentum	$H_{\text{CMG}}$	70 N·m·s
Flywheel spinning speed	$\Omega$	$316\pi$ rad/s
Mass	$m_{\text{CMG}}$	26 kg
Offset	$h$	0,172 m

Pointing direction of the flywheel rotation axis and arrangement of the eight-axis test board and the CMG is shown in Fig. 8. The original point of test board coordinate system is the centre of the bearings bridge assembling plate, and the direction of the test board and CMG coordinate system is displayed in the figure below. And the direction that the CMG gimbal angles are rotating clockwise is the positive one. As shown in Fig. 8, the  $O_t y_t$ -axis parallels to the gimbal axis. And between the centre of test table and the origin  $O_t$  that coincides with  $O_t x_t y_t z_t$ , there is an offset  $b$  along the  $OY$ -axis. According to the relationship between the  $O_t x_t y_t z_t$  and  $OXYZ$ , the distance vector  $r$ , could be expressed as

$$r_{O_t x_t y_t z_t} = [0 \ b \ -h]. \quad (31)$$

#### 3.2 Rigid eight-axis test board

The rigid eight-axis test board is implemented in the experiment, as shown in Fig. 9. Considering all the disturbance payloads need to be measured between the moving parts and mounting plate in this experiment, which includes three translational forces, two bending moments and a torque, it is necessary for the sensors to collect disturbance signal from all directions of the space. Therefore, a rigid eight-axis test board is designed for it, with eight high precision piezoelectric sensors screw-mounted in the box. Screw-mounting the CMG to the mounting plate, and piezoelectric sensors would transfer the disturbance signal to voltage signal, and then data collecting system would gather and analyse the signals to get the payloads of the disturbance source.

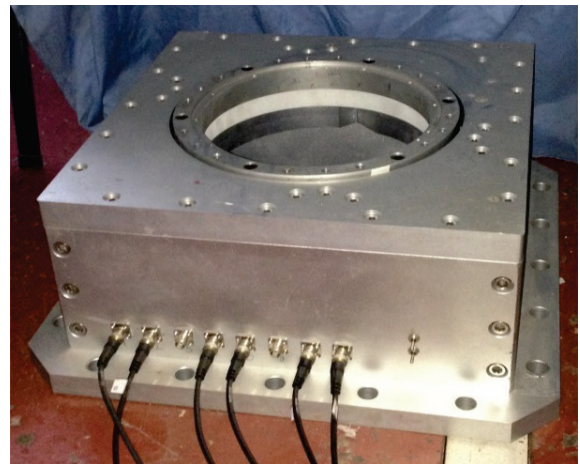


Figure 9 The eight-axis micro-vibration measuring system components

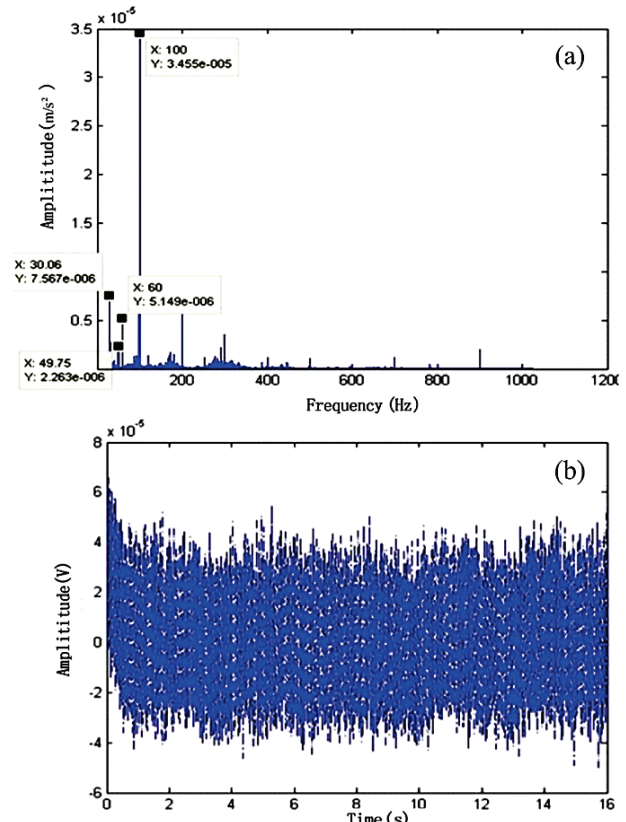


Figure 10 (a) Frequency domain of No. 1 background sensor; (b) Time domain of No. 1 background sensor

**Table 2** Parameters of the eight-axis test board system

Measuring range (Dynamic force)	$(0.5 \times 10^{-3} \div 5 \times 10^2)$ N
Frequency scope	(0.5 $\div$ 1024) Hz
Resolution rate of the disturbance (force, torque)	$10^{-3}$ N, $10^{-3}$ N·m
Phase 1 frequency of test board (dead load)	678 Hz

### 3.3 Background noise

The effective measurement range is determined to set as follows: force is bigger than 0,001 N at (0,5  $\div$  1000) Hz; moment is bigger than 0,001 N·m at (0,5  $\div$  1000) Hz.

As shown in the graphs (Fig. 10), the voltage magnitude of the background noise is  $10^{-5}$  V. Meanwhile, the voltage magnitude of the CMG test vibration is  $10^{-3}$  V. SNR is bigger than 40 dB, which means the experiment environment fulfils all the requirements.

### 3.4 Data processing

By implementing the data collecting and processing system, the disturbance payloads of the disturbing source could be calculated from the voltage signals. The equation used to transfer the voltage signal to force signal is:

$$F_{6 \times 1} = W_{6 \times 8} \cdot V_{8 \times 1}. \quad (32)$$

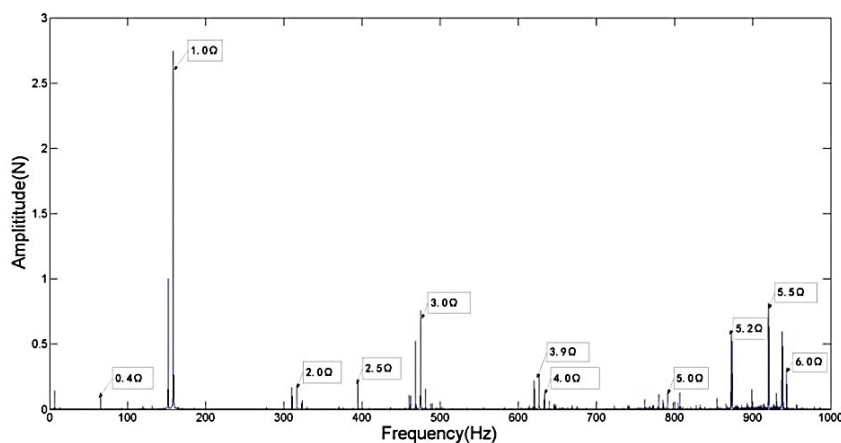


Figure 11 Steady-state test vibration disturbance of  $F_x$  (9500 r/min)

For the measured first natural frequency of the testing board, with the CMG bridge mounting, is 547 Hz, the CMG would couple with the testing board when the test frequency exceeds 500 Hz. It is impossible to recognize the natural frequency of CMG and its mounting structure in this situation. Therefore, only natural frequencies within 500 Hz could be measured from the test. From the waterfall figure of the start process test, the ridges of the disturbance frequency in proportion to the rotation speed could be recognized, which are corresponding to the disturbance of different harmonic waves number. There are four ridges with disturbance frequencies unrelated to the rotation speed around 310 Hz, 370 Hz, 456 Hz and 470 Hz, which should be caused by internal CMG axial and radial translational disturbance modal. Meanwhile, there are several obviously 'V' like disturbances, which is the distinct feature of the flywheel vacillation. And the two branches of 'V' are respectively the negative and positive movement branch of the vacillation modal. The

The 6 components of the vector  $F_{6 \times 1}$  are disturbing force components, and 8 components of the vector  $V_{8 \times 1}$  are the output signals of the sensors.  $W_{6 \times 8}$  is the calibrating matrix, and is developed from calibrating principle and liner system identification [25]. All the output of the eight channels would be decoupled by the calibration matrix, and transfer the voltage signal to the force signal.

Fig. 11 shows the frequency components of typical rotational speed when CMG rotates at 9500 r/min. The amplitudes of fundamental harmonic are larger than that of higher harmonics.

## 4 Results and discussion

### 4.1 Natural frequencies

The natural frequencies of the measurement system significantly affect the micro-vibration test results. A measuring method combined hammering and start process test, hence, is raised according to the features of CMG. Firstly, measuring the static natural modal of CMG and the mounting structure frequency; then implementing the start process test by measuring all the structural frequencies corresponding to gradually increase CMG rotation speed. Finally, the natural frequency of working CMG could be measured with all the frequencies obtained from the above process.

natural frequency of the negative movement would decrease along with the rise of the rotation speed. Accordingly, the natural frequency of the positive movement would rise with it. The values of CMG natural frequencies are shown in Tab. 3.

Table 3 CMG Natural frequency (0  $\div$  500 Hz)

Frequency unrelated to rotation	V line frequency
309	174 (0 rpm) to 151 (9500 rpm)
367	174 (0 rpm) to 316 Hz (9500 rpm)
456	
467	

In addition to the inherent frequency of CMG and its installation that exerts influence on CMG's vibration disturbance characteristic, rotation speed parameter (gimbal angle  $\delta$  and rotation speed  $\dot{\delta}$ ) is the other factor. In order to measure the influence of these two factors, two

tests of steady-state test and dynamic-state test were designed respectively. The former one was used to identify gimbal angle's influence on CMG's vibration

disturbance characteristic, while the latter one was used to measure both gimbal angle and rotation speed's influence on CMG's vibration disturbance characteristic.

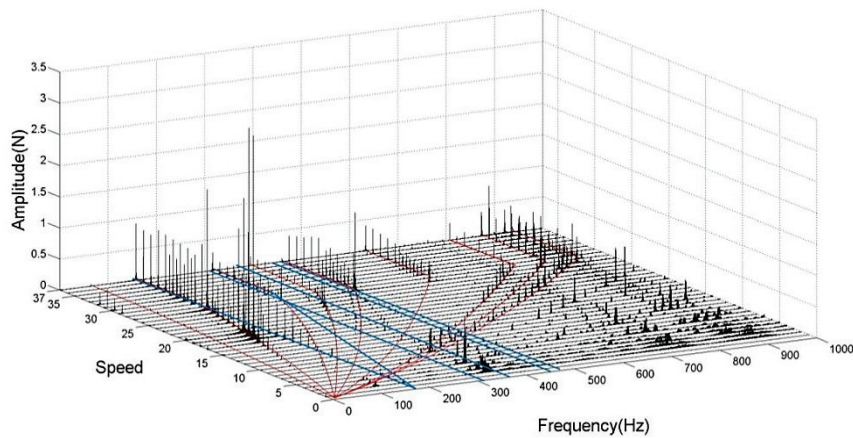


Figure 12 CMG start-up test vibration disturbance  $F_x$  waterfall figure

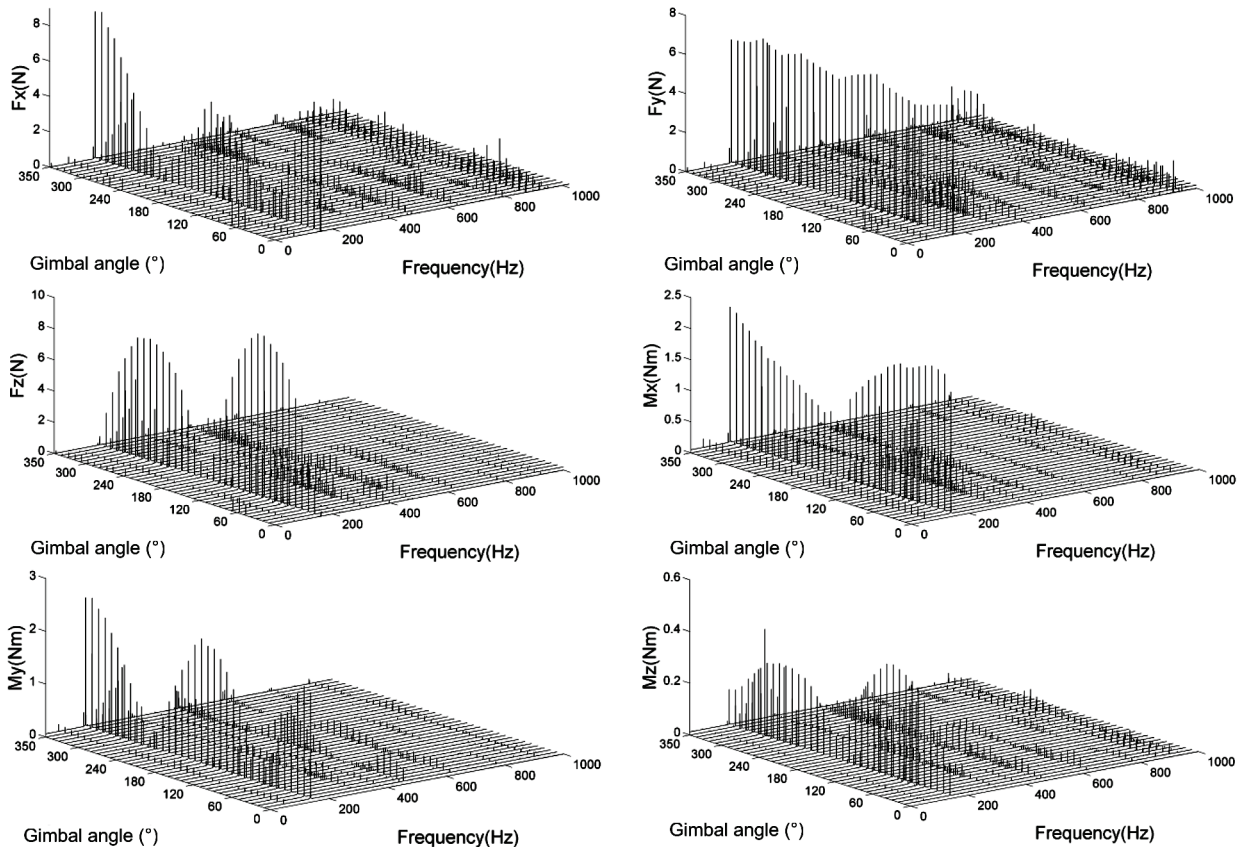


Figure 13 Steady-state test vibration disturbance waterfall figures

#### 4.2 Steady-state test of CMG's vibration disturbance characteristics

During the steady-state test, the gimbal is stationary. The rated speed of the rotor is 9500 rpm. Every  $10^\circ$  of gimbal angle from  $0^\circ$  to  $350^\circ$  is a measuring point, and altogether 36 operation modes were measured. Fig. 14 plots the datasets in three dimensions, illustrating that the disturbance amplitudes and the frequency spectrums vary with the gimbal angles. From the figures, it is clear that the overall disturbance outputs of the CMG in each component axis are closely related to the gimbal angles. When the gimbal stands still, micro-vibrations of the

spinning flywheel become the only disturbance source for the CMG. The output forces of a spinning flywheel are caused by static imbalance. From Eqs. (8) and (18):

$$\begin{cases} f_{gx} = m\ddot{x} = m_s R \Omega^2 \cos \Omega t - k_f x \\ f_{gy} = m\ddot{y} = m_s R \Omega^2 \sin \Omega t - k_f y \\ f_{gz} = m\ddot{z} = \sum_{i=1}^{\infty} F_{rz_i} e^{j i \Omega t} \end{cases} \quad (33)$$

From Fig. 13, there are only small changes in the output force of  $Y$  axial fundamental frequencies amplitude, which could be possibly due to the rigidity of flywheel bearings. The output force of  $X$  and  $Z$  axial fundamental amplitude conforms to the below functions:

$$\frac{\|F_z\|}{\|F_x\|} = \tan \delta. \quad (34)$$

Generally, the dynamic imbalance of rotating flywheel would produce the direct output torque. Since the flywheel is suspended by the gimbal system in the tests, the output torques shown in Fig. 13 consist of both the direct part induced by the dynamic imbalance and the indirect part which originates from disturbance forces multiplied by the distances  $h$  or  $b$  shown in Fig. 8.

#### 4.3 Dynamic-state test of CMG's vibration disturbance characteristics

The gimbal angle velocity varies from  $1^\circ/\text{s}$  to  $60^\circ/\text{s}$ . A waterfall plot can be created by overlaying the vibration disturbance signals' change with gimbal angle's change. The rotation disturbance feature of  $Y$  direction is the key analysis of this study. Fig. 14(a) is the slice figure of  $F_y$  under the rotation speed  $\dot{\delta} = 10^\circ/\text{s}$ , and Fig. 14(b) is the water fall graph of  $F_y$ .

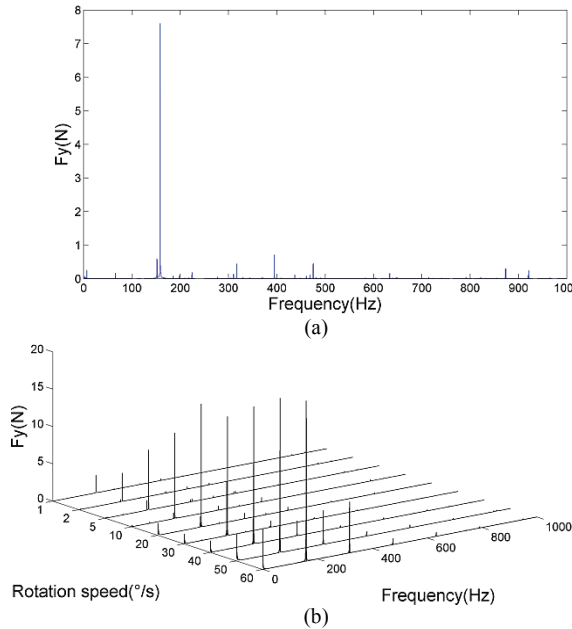


Figure 14 (a)  $F_y$  under the rotation speed  $\dot{\delta} = 10^\circ/\text{s}$  (b) waterfall graph of  $F_y$

The rotation disturbance response of  $Y$  direction of CMG, the frame axial direction, is quite complicated. While the frame is rotating, there are two sources of rotary disturbance along the specific direction, which includes the excitement of rotor output and disturbance of the frame system. We can see from the Eq. (30):

$$J_{gyy}\ddot{\phi} = J\ddot{\beta} - 2J\Omega\dot{\alpha} + T_{friction}\Omega_g + T_{ripple}\dot{\phi} + T_{input}\Omega_g, \quad (35)$$

and from Eqs. (26), (27) and (30):

$$\begin{aligned} J_{gyy}\ddot{\phi} &= J\ddot{\beta} - 2J\Omega\dot{\alpha} - c_{xz}\dot{\phi} + T_{input}\Omega_g + \\ &+ T_\alpha \sin \frac{n_m}{p_m} \Omega_g t - T_r(\kappa_5 - \kappa_7) \cos 6\Omega_g t, \end{aligned} \quad (36)$$

where  $c_{xz}$  is the rotary friction coefficient of output bearing;  $\Omega_g$  is the angular speed of the frame.

Due to the disturbance response of bearings damping is produced instantaneously, it would be weakening over time. So this kind of disturbance response could be excluded while studying the steady response of execution mechanism, then the disturbance response along the  $Y$  direction would be:

$$\begin{aligned} \dot{\phi} &= -\frac{c_{xz}T_\alpha}{\frac{n_m}{p_m}\Omega_g \left[ c_{xz}^2 + \left( J_{gyy} \frac{n_m}{p_m} \Omega_g \right)^2 \right]} \cos \frac{n_m}{p_m} \Omega_g t + \\ &+ \frac{J_{gyy}T_r(\kappa_5 - \kappa_7)}{c_{xz}^2 + 36(J_{gyy}\Omega_g)^2} \cos 6\Omega_g t - \\ &- \frac{c_{xz}T_\alpha}{\left[ c_{xz}^2 + \left( J_{gyy} \frac{n_m}{p_m} \Omega_g \right)^2 \right]} \sin \frac{n_m}{p_m} \Omega_g t - \\ &- \frac{c_{xz}T_r(\kappa_5 - \kappa_7)}{6\Omega_g [c_{xz}^2 + 36(J_{gyy}\Omega_g)^2]} \sin 6\Omega_g t + \\ &+ T_{input}\Omega_g + J\ddot{\beta} - 2J\Omega\dot{\alpha} \end{aligned}. \quad (37)$$

The rotation disturbance responses of CMG  $Y$  axial are mainly produced in the form of harmonic waves, therefore, the driving torque of low speed driving motor could not be ignored. From Fig. 14(b), the rotation speed of the frame is obviously correlated to the amplitude of low frequency. The amplitude of fundamental frequency is increasing with the increase of the rotation speed. Furthermore, the frame and flywheel bearing supporting rigidity is changing according to the gimbal angles, which would exert certain impact to the amplitude of fundamental frequency. In all, the fundamental frequency amplitude would be affected by rotation speed and gimbal angles at the same time.

#### 5 Conclusions

By establishing the kinetics model of CMG with Euler equations, this paper studied the disturbance features of CMG and had some new findings. The fact that overall distance outputs of the CMG in each component axis are highly dependent on the gimbal angles was proved by an experimental test conducted later to measure the disturbances produced by an off-the-shelf CMG. The rotor is the substantial core institution to store the angular momentum, meanwhile, it is the major source of high frequency disturbance produced by the execution institution. High frequency disturbances are the majorities among the disturbances, in which the fundamental frequencies disturbance is usually bigger than multiplication frequencies. The disturbances of CMG are mainly performed in the form of harmonic waves, and

could be separated as translational and rotational disturbances. The translational disturbances mainly consist of harmonic waves, which are generated from the imbalance of the flywheel. The higher harmonics mainly consist of the harmonic wave disturbances from the mutual movements of each bearing components. The rotation disturbances frequencies are relatively complicated, including the low frequencies disturbances from gimbal retainer. The rotational disturbances are similar to the translational disturbances in  $X$  direction, which consist of harmonic waves; there are two disturbance sources in  $Y$  direction, which include the rotor output excitement disturbances and the gimbal system disturbances; the  $Y$  axis rotational disturbances are free vibration, which are transient process, and it would vanish due to the damping. Finally, the kinetics model is proved to be valid through the experiment, and it could be implemented to analyse the disturbance features of CMG.

## 6 References

- [1] Luo, Q.; Li, D. X.; Zhou, W. Y. Dynamic modelling and observation of micro-vibrations generated by a Single Gimbal Control Moment Gyro. // Journal of Sound and Vibration. 332, 19(2013), pp. 4403-4424.
- [2] Eyeran, C. E. A System Engineering Approach to Disturbance Minimization for Spacecraft Utilizing Controlled Structures Technology, Master Degree Thesis, Aeronautics and Astronautics, MIT, 1990.
- [3] Shigemune, T.; Masahito, K.; Makoto, S.; Yoshiaki, O. Analysis of retainer induced disturbances of reaction wheel. // Journal of System Design and Dynamics. (2007), pp. 307-317. <http://dx.doi.org/10.1299/jbdd.1.307>.
- [4] Zhou, W. Y.; Li, D. X.; Luo, Q.; Liu, K. Analysis and testing of micro vibrations produced by momentum wheel assemblies. // Chinese Journal of Astronautics. 25, (2012), pp. 640-649. <http://dx.doi.org/10.1016/s1000-9361.1160430-5>.
- [5] Davis, L. P.; Wilson, J. F.; Jewell, R. E.; Roden, J. J. Hubble Space Telescope Reaction Wheel Assembly Vibration Isolation System, NASA Marshall Space Flight Centre, 1986.
- [6] Shigemune, T.; Yoshiaki, O. Experimental and numerical analysis of reaction wheel disturbances. // JSME International Journal, Series C 46, (2003), pp. 519-526.
- [7] Masterson, R. A.; Miller, D. W.; Grogan, R. L. Development and validation of empirical and analytical reaction wheel disturbance models. // Proceedings of the 1999 AIAA/ASME/ASCE/AHS/ASC Structures, Structural Dynamics and Materials Conference / St. Louis MO, 1999.
- [8] Masterson, R. A.; Miller, D. W.; Grogan, R. L. Development and validation of reaction wheel disturbance models: empirical model. // Journal of Sound and Vibration. 249, (2002), pp. 575-598.
- [9] Narayan, S. S.; Nair, P. S.; Ghosal, A. Dynamic interaction of rotating momentum wheels with spacecraft elements. // Journal of Sound and Vibration. 315, 4-5(2008), pp. 970-984.
- [10] Pang, S. W.; Yang, L.; Xu, G. J. New Development of Micro-vibration Integrated Modeling and Assessment Technology for High Performance Spacecraft. // Structure & Environment Engineering. 34, 6(2007).
- [11] Chang, B. Q.; Qing, X.Y. Dynamic model of ball bearings with internal clearance and waviness. // Journal of Sound and Vibration. 294, (2006), pp. 23-48.
- [12] Elias, L. M.; Miller, D. W. A coupled disturbances analysis method using dynamic mass measurement techniques. //
- AIAA/ASME/ASCE/AHS/ASC Structures, Structural Dynamics, and Materials Conference. 2002; 2002-1252.
- [13] Shigemune, T.; Masahito, K.; Makoto, S.; Yoshiaki, O. Analysis of retainer induced disturbances of reaction wheel, // Transactions of the Japanese Society of Mechanical Engineering. 71, 1(2005), pp. 21-28.
- [14] Zhou, W. Y.; Aglietti, G. S.; Zhang, Z. Modeling and testing of a soft suspension design for a reaction/momentum wheel assembly. // Journal of Sound and Vibration. 330, 28(2011).
- [15] Zhou, W. Y.; Li, D. X. Design and analysis of an intelligent vibration isolation platform for reaction/ momentum wheel assemblies. // Journal of Sound and Vibration. 331, 13(2012), pp. 2984-3005.
- [16] Vaillon, L.; Philippe, C. Passive and active micro-vibration control for very high pointing accuracy space systems. // Smart Materials and Structure. 8, (1999), pp. 719-728.
- [17] Riper, R. V. Future technology trends for control moment gyroscopes, Proceedings of AIAA Guidance, Navigation and Control Conference, Williamsburg, VA, April 1986.
- [18] Harris, T. A.; Kotzalas, M. N. Rolling Bearing Analysis, fifth ed.: Essential Concepts of Bearing Technology, Taylor & Francis Group LLC, New York, 2007.
- [19] Jang, G. H.; Jeong, S. W. Nonlinear excitation model of ball bearing waviness in a rigid rotor supported by two or more ball bearings considering five degrees of freedom. // Journal of Tribology. 124, (2002), pp. 82-90.
- [20] Harsha, S. P. Non-linear dynamic response of a balanced rotor supported on rolling element bearings. // Mechanical Systems and Signal Processing. 19, 3(2005), pp. 551-578.
- [21] Lim, T. C.; Singh, R. Vibration transmission through rolling element bearings, Part 1: bearing stiffness formulation. // Journal of Sound and Vibration. 139, 2(1990), pp. 179-199.
- [22] Lim, T. C.; Singh, R. Vibration transmission through rolling element bearings, Part 1: system studies. // Journal of Sound and Vibration. 1990, 139(2), pp. 201-225.
- [23] SNFA, Precision ball bearing assembly manual and bearing damage analysis. [http://www.skf.com/iec\\_documents/Assembly\\_manual\\_english\\_version.pdf](http://www.skf.com/iec_documents/Assembly_manual_english_version.pdf).
- [24] Wu, Z.; Wu, H. X. Analysis and Attenuation of Disturbance Torque in SGCMG Gimbal Servo Systems. // Aerospace Control. 16, 4(1998).
- [25] Liu, D. H. Methods and application of System identification. National defence industrial press, 2010.

## Authors' addresses

### Xue Li, grades and ranks

School of Aeronautical Science and Engineering  
Beihang University  
NO. 37, Xueyuan Road, Beijing 100191, China  
E-mail: daxue129.student@sina.com

### Wei Cheng,

School of Aeronautical Science and Engineering  
Beihang University  
NO. 37, Xueyuan Road, Beijing 100191, China  
E-mail: 2cheng\_wei@buaa.edu.cn

### Xiongfei Li, grades and ranks

School of Aeronautical Science and Engineering  
Beihang University  
NO. 37, Xueyuan Road, Beijing 100191, China  
E-mail: daxue1984@sohu.com